The Astrophysical Journal, 982:196 (8pp), 2025 April 1 https://doi.org/10.3847/1538-4357/adbbde


# Revisiting X-Ray Afterglows of Jetted Tidal Disruption Events with the External Reverse Shock

Chengchao Yuan (袁成超)[1], Walter Winter[1], B. Theodore Zhang (张兵)[2,3], Kohta Murase[4,5], and Bing Zhang (张冰)[6,7]
[1] Deutsches Elektronen-Synchrotron DESY, Platanenallee 6, 15738 Zeuthen, Germany; chengchao.yuan@desy.de
[2] Key Laboratory of Particle Astrophysics, Institute of High Energy Physics, Chinese Academy of Sciences, Beijing 100049, People's Republic of China
[3] TIANFU Cosmic Ray Research Center, Chengdu, People's Republic of China
[4] Department of Physics, Department of Astronomy & Astrophysics, Center for Multimessenger Astrophysics, Institute for Gravitation and the Cosmos, The Pennsylvania State University, University Park, PA 16802, USA
[5] Center for Gravitational Physics and Quantum Information, Yukawa Institute for Theoretical Physics, Kyoto University, Kyoto, Kyoto 606-8502, Japan
[6] The Nevada Center for Astrophysics, University of Nevada, Las Vegas, Las Vegas, NV 89154, USA
[7] Department of Physics and Astronomy, University of Nevada, Las Vegas, Las Vegas, NV 89154, USA
*Received 2024 November 14; revised 2025 February 18; accepted 2025 March 1; published 2025 March 31*

## Abstract

We investigate the external reverse shock (RS) region of relativistic jets as the origin of X-ray afterglows of jetted tidal disruption events (TDEs) that exhibit luminous jets accompanied by fast-declining nonthermal X-ray emissions. We model the dynamics of jet propagating within an external density medium, accounting for continuous energy injection driven by accretion activities. We compute the time-dependent synchrotron and inverse Compton emissions from the RS region. Our analysis demonstrates that the RS scenario can potentially explain the X-ray light curves and spectra of four jetted TDEs, namely, AT 2022cmc, Swift J1644, Swift J2058, and Swift J1112. Notably, the rapid steepening of the late-stage X-ray light curves can be attributed jointly to the jet break and cessation of the central engine as the accretion rate drops below the Eddington limit. Using parameters obtained from X-ray data fitting, we also discuss the prospects for $\gamma$-ray and neutrino detection.

*Unified Astronomy Thesaurus concepts:* Tidal disruption (1696); Relativistic jets (1390); Transient sources (1851); Radiative processes (2055)

## 1. Introduction

Tidal disruption events (TDEs) occur when a star is torn apart by the tidal forces of a supermassive black hole (SMBH; e.g., J. G. Hills 1975; M. J. Rees 1988; C. R. Evans & C. S. Kochanek 1989), resulting in a transient lasting from months to years, visible across the electromagnetic spectrum, from the radio, infrared, optical/ultraviolet, to X-ray ranges (e.g., K. D. Alexander et al. 2020; R. Saxton et al. 2020; S. van Velzen et al. 2021). A small fraction of TDEs exhibit luminous relativistic jet signatures. Since the discovery of the hard X-ray transient event J164449.3+573451 (hereafter, Sw J1644; J. S. Bloom et al. 2011; D. Burrows et al. 2011; A. J. Levan et al. 2011; B. A. Zauderer et al. 2011) by the Swift satellite, three additional jetted TDEs—Swift J2058.4+0516 (hereafter, Sw J2058; S. B. Cenko et al. 2012; D. R. Pasham et al. 2015), Swift J1112.2-8238 (hereafter Sw J1112; G. C. Brown et al. 2015; G. C. Brown et al. 2017), and AT 2022cmc (I. Andreoni et al. 2022; D. R. Pasham et al. 2023)—have been recorded. The multiwavelength observations of these four jetted TDEs have provided valuable prototypes for studying the radiation mechanisms, accretion histories, and jet dynamics over a time window of months to years (e.g., D. Giannios & B. D. Metzger 2011; F. De Colle & W. Lu 2020; J. L. Dai et al. 2021; C. Yuan et al. 2024b).

The four jetted TDEs exhibit prominent similarities in their X-ray and radio afterglows. The X-ray light curves can be roughly described by a power-law decay, with the index roughly ranging from 5/3 (e.g., Sw J1644; V. Mangano et al. 2016) to 2.2 (e.g., Sw J2058 and AT 2022cmc; T. Eftekhari et al. 2024). Late-time follow-up observations have revealed additional steepening in the X-ray light curves, suggesting common changes in jet evolution or the central engine (B. A. Zauderer et al. 2013; D. R. Pasham et al. 2015; T. Eftekhari et al. 2024). Additionally, the rapid variability on timescales of $\sim$few $\times$ 100–1000 s imposes further constraints on the SMBH mass (G. C. Brown et al. 2015; V. Mangano et al. 2016; D. R. Pasham et al. 2023; Y. Yao et al. 2024), e.g., $\lesssim$few $\times 10^7 M_\odot$. In the radio and submillimeter bands, observations have shown that these emissions are typically long-lasting compared to the fast-declining X-ray emission. The radio/submillimeter light curves are consistent with synchrotron radiation from electrons accelerated by the external forward shock (FS) of the jet with a Lorentz factor of $\Gamma \sim$ 1–10 propagating through a circumnuclear medium (CNM; e.g., D. Giannios & B. D. Metzger 2011; B. A. Zauderer et al. 2011; E. Berger et al. 2012; B. D. Metzger et al. 2012; B. A. Zauderer et al. 2013; Q. Yuan et al. 2016; T. Eftekhari et al. 2018; Y. Cendes et al. 2021; T. Matsumoto & B. D. Metzger 2023; C. Yuan et al. 2024b; C. Zhou et al. 2024). However, the origin of jetted TDE X-ray afterglows still remains unclear.

The X-ray emission from jetted TDEs is likely produced in a separate emission region. Theoretical models involving jets powered by SMBH spin energy via large-scale magnetic fields (L. Z. Kelley et al. 2014; A. Tchekhovskoy et al. 2014), energy dissipation within magnetically dominated jets (D. Burrows et al. 2011), variable accretion near the SMBH horizon (R. C. Reis et al. 2012), jet shell collisions (Y. C. Zou et al. 2013) and internal dissipations (F. Y. Wang & K. S. Cheng 2012; W.-H. Lei et al. 2013, 2016), inverse Compton scattering of external photons (J. S. Bloom et al. 2011; P. Crumley et al.

2016), and synchrotron emission (Y. Yao et al. 2024) have been investigated to explain the X-ray observations of jetted TDEs. The power-law decaying X-ray light curves align with the mass fallback rates from complete ($t^{-5/3}$; e.g., M. J. Rees 1988; E. S. Phinney 1989) and partial ($t^{-2.2}$; e.g., J. Guillochon & E. Ramirez-Ruiz 2013) disruptions. The late-stage sharp steepening of the X-ray light curves may result from jet shutoff, caused by the accretion disk transitioning from thick to thin as the accretion rate decreases from super- to sub-Eddington states (B. A. Zauderer et al. 2013; A. Tchekhovskoy et al. 2014). R.-F. Shen & C. D. Matzner (2014) suggest that the accretion rate may undergo a dramatic drop at that time the accretion disk becomes radiatively cooling and gas-pressure dominated.

Moreover, a two-component jet model with a fast inner component and slow outer component has also been exploited to explain the multiwavelength emission from TDEs (J.-Z. Wang et al. 2014; D. Liu et al. 2015; P. Mimica et al. 2015; O. Teboul & B. D. Metzger 2023; Y. Sato et al. 2024; C. Yuan et al. 2024b). Recently, C. Yuan et al. (2024b) suggested that the external reverse shock (RS) powered by a relativistic jet launched from the active central engines, such as continuous energy injection associated with accretion, can also explain the X-ray observations of AT 2022cmc, where the late-time rapid decay can be attributed to jet breaks. This is also analogous to the long-lasting RS model for shallow-decay afterglow emission of $\gamma$-ray bursts (GRBs).

Following C. Yuan et al. (2024b), we investigate the external RS scenarios to explain the X-ray spectra and light curves of the four jetted TDEs, focusing on the fast jet scenario with $\Gamma > 10$, whereas a slow jet (e.g., $\Gamma \lesssim 5$) may be responsible for the radio emission. We present a generic, self-consistent model based on the TDE accretion history and multiwavelength observations to describe the jet evolution and the time-dependent emissions in jet RS regions. The motivation is that jet deceleration, combined with an active central engine, jointly determines the RS emission, which can naturally reproduce the $t^{-\delta}(\delta \sim 5/3\text{–}2.2)$ X-ray afterglows. Additionally, the cessation of power injection would result in sharply decaying RS emission.

We model the time-dependent accretion rate, jet evolution within an external medium incorporating continuous power injection, and RS emission in Section 2. In Section 3, we apply the RS model to fit the X-ray light curves and spectra of four jetted TDEs and discuss the $\gamma$-ray and neutrino detectabilities. We discuss and conclude our work in Sections 4 and 5.

Throughout the paper, we use $T_{\rm obs}$, $t$, and $t'$ to denote the times measured in the observer's frame, the SMBH-rest frame, and the jet comoving frame, respectively.

## 2. TDE Jet and RS Modeling

### 2.1. Accretion History

Considering a TDE originated from the disruption of a main-sequence star of mass $M_\star$ by a SMBH of mass $M_{\rm BH}$, we write down the critical tidal radius $R_{\rm T} = f_{\rm T}\,(M_{\rm BH}/M_\star)^{1/3}R_\star$ (e.g., M. J. Rees 1988), where $f_{\rm T} \sim 0.02\text{–}0.3$ represents the correction from the stellar structures (e.g., E. S. Phinney 1989; T. Piran et al. 2015) and $R_\star$ is the radius of the star. After the disruption, approximately half of the star's mass remains bound within an eccentric orbit. A fraction ($\eta_{\rm acc}$) of the bounded mass will end up being accreted by the SMBH. The fallback time can be estimated as the orbital period of most tightly bound matter, e.g., $t_{\rm fb} \approx 2\pi\sqrt{a_{\rm min}^3/GM_{\rm BH}} \simeq 3.3 \times 10^6\,{\rm s}\, f_{\rm T,-1.2}^{1/2} M_{\rm BH,7}^{1/2} M_{\star,0.7}^{-1/10}$ (e.g., K. Murase et al. 2020), where $a_{\rm min} \approx R_{\rm T}^2/(2R_\star)$ is the semimajor axis of the orbit and the stellar mass–radius relationship $R_\star = R_\odot (M_\star/M_\odot)^{1-\xi}$ (R. Kippenhahn & A. Weigert 1990) with $\xi \sim 0.4$ in the mass range $1 < M_\star/M_\odot < 10$ is adopted. Here, we chose $f_{\rm T} = 10^{-1.2}$ as the fiducial value and scale $t_{\rm fb}$ to the value for AT 2022cmc, $M_\star = 5M_{\star,0.7}M_\odot$ (C. Yuan et al. 2024b), for illustration purposes.

Using $t_{\rm fb}$ and $\eta_{\rm acc}$, and considering that the postfallback accretion rate follows a power law of $t^{-5/3}$, we express the time-dependent accretion rate as (C. Yuan et al. 2024b)

$$\dot{M}_{\rm BH} = \frac{\eta_{\rm acc} M_\star}{} \times \begin{cases} \left(\frac{t}{t_{\rm fb}}\right)^{-\alpha}, & t < t_{\rm fb} \\ \left(\frac{t}{t_{\rm fb}}\right)^{-5/3}, & t > t_{\rm fb} \end{cases}, \tag{1}$$

where $0 \leqslant \alpha < 1$ is the early-time accretion index,[8] and $\mathcal{C} = 3 + 2/(1-\alpha)$ is the normalization coefficient. We then parameterize the power reprocessed to the relativistic jet from the mass accretion using the energy conversion efficiency $\eta_j$,

$$L_j = \eta_j \dot{M}_{\rm BH} c^2. \tag{2}$$

The accretion and jet power efficiencies, $\eta_{\rm acc}$ and $\eta_j$, remain uncertain as they depend on the dynamics of mass fallback, disk formation, and the magnetic flux accumulation (e.g., K. Murase et al. 2020). Meanwhile, $\eta_j$ may depend on the accretion rate and the SMBH spin (see, e.g., W.-H. Lei et al. 2017); for simplicity, we assume it to be constant. Noting that these two parameters are degenerate with the stellar mass in terms of data fitting, we define the total jet energy as $\mathcal{E}_j = \int L_j dt = \eta_j \eta_{\rm acc} M_\star c^2/2$, which, instead of $\eta_j$ and $\eta_{\rm acc}$, will be treated as a free parameter.

### 2.2. Jet Dynamics

It is useful to define a generic density profile of the external medium through which the relativistic jets propagate and decelerate. The interpretation of radio observations using the FS model demonstrates that the density profile as a function of the distance to the SMBH ($R$), $n \propto R^{-k}$ with $1.5 < k < 2.0$, is favored (e.g., T. Matsumoto & B. D. Metzger 2023; Y. Yao et al. 2024; C. Zhou et al. 2024), while the analysis of radio emissions in nonjetted TDEs suggests a little steeper profile $k = 2.5$ (e.g., K. D. Alexander et al. 2020). Fitting the X-ray spectra and light curves of AT 2022cmc indicates that a fast jet with a Lorentz factor of $\Gamma = {\rm few} \times 10$ is typically needed (C. Yuan et al. 2024b), implying that the jet could penetrate the CNM and reach the interstellar medium (ISM). Therefore, we follow C. Yuan et al. (2024b), and connect the CNM to the ISM, which yields

$$n_{\rm ext} = \begin{cases} n_{\rm ISM}\left(\frac{R}{R_{\rm cnm}}\right)^{-k}, & R < R_{\rm cnm} \\ n_{\rm ISM}, & R > R_{\rm cnm}. \end{cases} \tag{3}$$

One possible source for the CNM within $R_{\rm cnm}$ is the wind emanating from preexisting disks, which predicts the boundary

[8] R.-F. Shen & C. D. Matzner (2014) pointed out that a slow-decaying accretion rate is possible due to disk internal kinematic viscosity, depending on the type of polytrope stars.

$R_{\rm cnm} \sim 10^{18}$ cm before merging into the ISM (C. Yuan et al. 2020, 2021). Moreover, the wind density profile can be smoothly connected to ISM at the Bondi radius (T. Matsumoto & T. Piran 2024), which predicts the similar $R_{\rm cnm}$ of $\sim 10^{18}$ cm for $M_{\rm BH} \sim 10^7 M_\odot$. The density profile within $R_{\rm cnm}$ primarily impacts jet evolution in the very early stage and does not significantly influence the results after $T_{\rm obs}\sim$ few days. In subsequent calculations, we adopt the fiducial values of $k = 1.8$ as in T. Matsumoto & B. D. Metzger (2023) and $R_{\rm cnm} = 10^{18}$ cm.

We follow the methodology for blastwave dynamics, as illustrated in GRB afterglow modeling (L. Nava et al. 2013; B. Zhang 2018; Y. Sato et al. 2024; B. T. Zhang et al. 2025) and the structured jet modeling of AT 2022cmc (C. Yuan et al. 2024b), to model the jet dynamics. The jet has a top-hat structure and points toward the observer (on-axis). Specifically, we examine how the jet Lorentz factor and radius depend on time, given the initial Lorentz factor $\Gamma_0$, the jet opening angle $\theta_j$, and $n_{\rm ext}$. In this picture, as the jet penetrates deeply into the ambient gaseous environment, it sweeps up material, leading to the formation of the FS, which accumulates and accelerates the upstream external medium to a Lorentz factor $\Gamma < \Gamma_0$. Meanwhile, an RS decelerates the unshocked ejecta from $\Gamma_0$ to $\Gamma$ within the jet.

For jetted TDEs, we consider a continuously powered jet, in the sense that the jet energy $\mathcal{E}_j$ and ejecta mass are persistently injected from the central engine. A comprehensive treatment of jet evolution incorporating the RS and continuous injections is presented in the Appendix of C. Yuan et al. (2024b). Here, we numerically solve the coupled differential equations derived in C. Yuan et al. (2024b). The results are consistent with the analytical solutions obtained from $\int L_j dt \propto \Gamma^2 m_p n_{\rm ext} c^2 R_j^3$ and $R_j \approx 2\Gamma^2 ct$,

$$\Gamma(t) \propto \begin{cases} t^{-(2+\alpha)/8}, & t < t_{\rm fb} \\ t^{-3/8}, & t > t_{\rm fb}, \end{cases} \tag{4}$$

where $R_j$ is the radius of the jet. In the following sections, the jet evolutions, specifically, $\Gamma(t)$ and $R_j(t)$, will be used to compute the time-dependent FS and RS emissions.

### 2.3. Multiwavelength Emission from RS Regions

We focus on the RS scenario, as C. Yuan et al. (2024b) have revealed that the fast-decaying X-ray afterglow of AT 2022cmc could be attributed to emissions generated in RS regions. Given the isotropic equivalent jet luminosity, $L_{j,iso} = L_j/(\theta_j^2/2)$, jet radius $R_j$, and Lorentz factor $\Gamma$, we estimate the relative Lorentz factor between the RS upstream and downstream, $\Gamma_{\rm rel} \approx (\Gamma_0/\Gamma + \Gamma/\Gamma_0)/2$, and the upstream particle number density $n_0' = L_{j,iso}/(4\pi R_j^2 \Gamma_0^2 m_p c^3)$ in the jet comoving frame. The downstream magnetic field strength can be parameterized as $B_{\rm rs} = \sqrt{32\pi \epsilon_B \Gamma_{\rm rel}(\Gamma_{\rm rel} - 1) n_0' m_p c^2}$, where $\epsilon_B$ represents the fraction of the internal energy density that is converted to magnetic field energy density.

We consider a power-law injection rate, $\dot{Q}_e \propto \gamma_e^{-s}$, to describe the distribution of nonthermal electrons accelerated by relativistic shocks. In this expression, $\gamma_e$ is the electron Lorentz factor and $s \geqslant 2$ is the spectral index. To normalize the injection rate, we introduce the number fraction ($f_e$) of downstream electrons that are accelerated by RS and the energy fraction ($\epsilon_e$) of internal energy that is converted to nonthermal electrons. This allows us to infer the minimum Lorentz factor of injected electrons, $\gamma_{e,\rm m} = (\Gamma_{\rm rel} - 1)(s-2)/(s-1)(\epsilon_e/f_e)(m_p/m_e)$ for $s > 2$, and normalize $\dot{Q}_e$. Using $B_{\rm rs}$, $\dot{Q}_e$, $R_j(t)$, and $\Gamma(t)$, we compute the time-dependent synchrotron and inverse Compton emissions in the synchrotron self-Compton (SSC) framework, and convert quantities in jet comoving frame to the observer's frame by integrating over the equal-arrival-time surfaces. We also account for the effect of jet break when the jet Lorentz factor drops below $1/\theta_j$ by applying $f_{\rm br} = 1/[1 + (\theta_j \Gamma)^{-2}]$ to the light curves.[9] This steepens the postbreak light curves after $t_{\rm br}$, defined by $\Gamma(t_{\rm br}) = 1/\theta_j$, with the factor $f_{\rm br} \propto \Gamma^2$ for $t > t_{\rm br}$. A detailed description of the numerical modeling of RS synchrotron and SSC emissions can be found in the Appendix.

**Table 1**
Physical Parameters ($f_e = 1.5 \times 10^{-3}$, $s = 2.3$, and $\epsilon_e = 0.2$ Are Fixed for All TDEs) and Results

| TDEs[a] | AT 2022cmc | J1644 | J2058 | J1112 |
|---|---|---|---|---|
| $z$ | 1.19 | 0.35 | 1.19 | 0.89 |
| $M_{\rm BH}$ ($M_\odot$) | $10^7$ | $10^6$ | $10^6$ | $2 \times 10^6$ |
| **Model Parameters** | | | | |
| $\alpha$ | 0.80 | 0.65 | 0.85 | 0.70 |
| $\mathcal{E}_j$ ($10^{52}$ erg) | 5.4 | 3.5 | 2.9 | 6.3 |
| $n_{\rm ISM}$ (cm$^{-3}$) | 10 | 6.0 | 1.0 | 10 |
| $\theta_j$ | 0.15 | 0.1 | 0.1 | 0.1 |
| $\Gamma_0$ | 30 | 25 | 42 | 35 |
| $\epsilon_B$ | 0.10 | 0.15 | 0.20 | 0.15 |
| **Results** | | | | |
| $M_\star$ ($M_\odot$)[b] | 3.0 | 1.9 | 1.6 | 3.5 |
| $T_{\rm fb}$ (d) | 77 | 28 | 27 | 21 |
| $T_{\rm br}$ (d) | 79 | 212 | 76 | 37 |
| $T_{\rm ce}$ (d)[c] | 227 | 352 | 331 | 470 |

**Notes.**
[a] Data sources: AT 2022cmc (I. Andreoni et al. 2022; D. R. Pasham et al. 2023), Sw J1644 (D. Burrows et al. 2011), Sw J2058 (D. R. Pasham et al. 2015), and Sw J1112 (G. C. Brown et al. 2015).
[b] The fiducial value $\eta_j \eta_{\rm acc} = 0.02$ is used to infer $M_\star$ from $\mathcal{E}_j$.
[c] The fiducial parameter $\eta_{\rm rad}\eta_{\rm acc} = 0.05$ is used to calculate the cessation time $T_{\rm ce} = (1 + z)t_{\rm ce}$ of the central engine. Please refer to the main text for the definitions of the fallback time $T_{\rm fb}$, the jet break time $T_{\rm br}$, and $T_{\rm ce}$.

## 3. RS Scenario for Four Jetted TDEs

### 3.1. X-Ray Data Interpretations

Table 1 summarizes the observational parameters, such as the redshifts and the SMBH masses,[10] for AT 2022cmc, Sw J1644 (J1644), Sw J2058 (J2058), and Sw J1112 (J1112). Noting that the masses of disrupted stars are not efficiently identified and can degenerate with the energy conversion efficiencies of accretion activities and jets, we treat the total jet energy $\mathcal{E}_j = \int L_j dt = \eta_j \eta_{\rm acc} M_\star c^2/2$ as a free parameter to infer the time-dependent jet power using Equations (1) and (2). Additionally, we select the accretion rate index $\alpha$ to model the X-ray light curves before the mass fallback time

[9] Here, we neglect the lateral spreading of the jet, known as the sideways expansion, for simplicity.
[10] The SMBH masses are poorly constrained. These fiducial values are chosen to satisfy the X-ray variability constraints (e.g., T. Eftekhari et al. 2024) and to ensure that the cessation times (defined later) are consistent with observations.

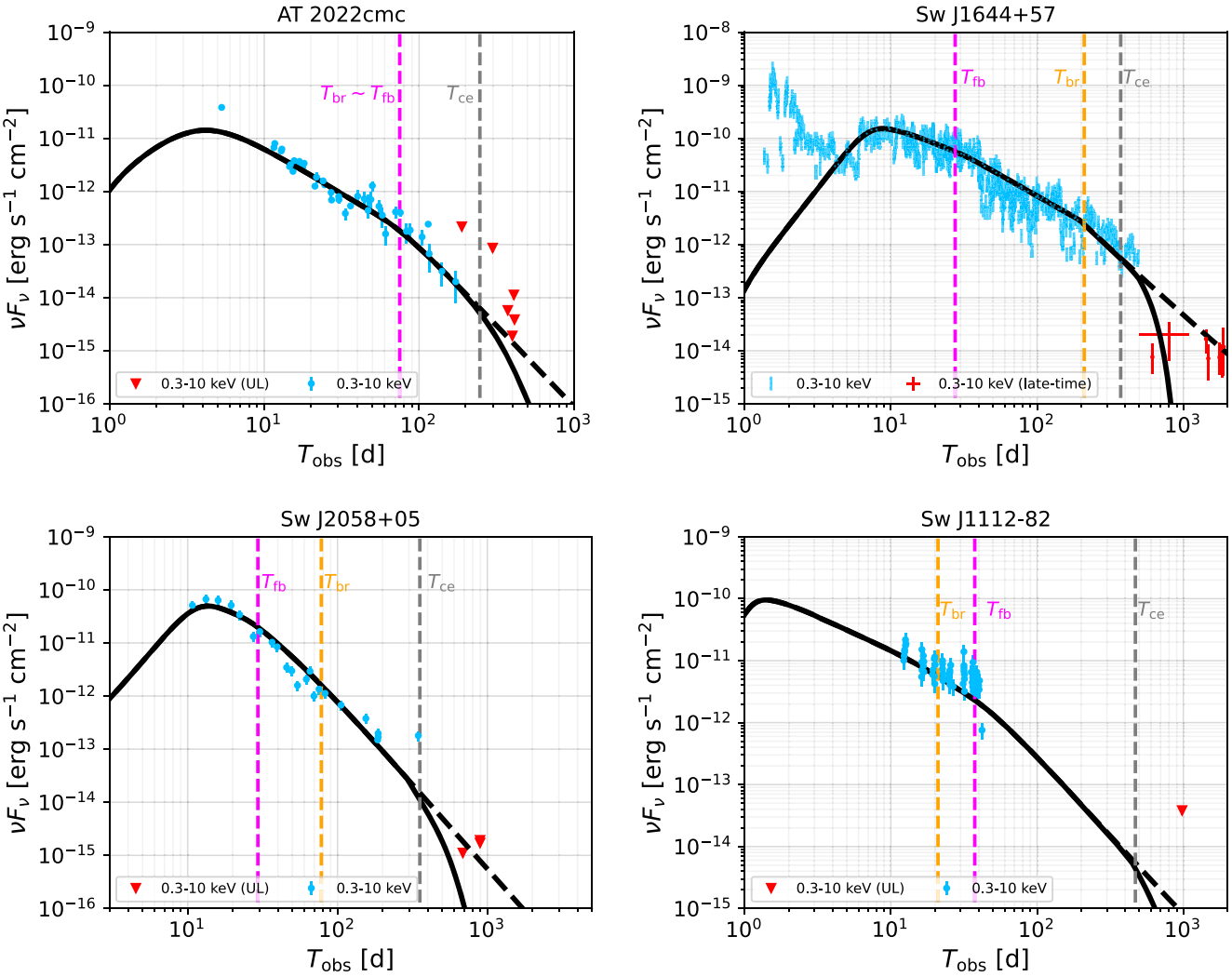


**Figure 1.** Swift 0.3–10 keV X-ray light curve fitting for four jetted TDEs. The early-stage and late-time data points (or upper limits) are shown as blue and red points (triangles). The dashed and solid black curves, respectively, depict the fitted X-ray light curves before and after accounting for the ceased central engine. The vertical dashed lines indicate the characteristic times obtained from the fitting, which are summarized in Table 1. Data sources: AT 2022cmc (I. Andreoni et al. 2022; D. R. Pasham et al. 2023; T. Eftekhari et al. 2024; Y. Yao et al. 2024), Sw J1644 (D. Burrows et al. 2011; B. A. Zauderer et al. 2013; V. Mangano et al. 2016; T. Eftekhari et al. 2018), Sw J2058 (D. R. Pasham et al. 2015), and Sw J1112 (G. C. Brown et al. 2015).

$T_{\rm fb} = (1+z)t_{\rm fb}$ and choose $n_{\rm ISM}$, $\theta_j$, and $\Gamma_0$ as fitting parameters to ensure that $T_{\rm fb}$ and jet break time $T_{\rm br} = (1+z)t_{\rm br}$ are consistent with the observed X-ray light curves (see the magenta and orange lines in Figure 1). For multiwavelength emissions from RS regions, we fix $f_e = 1.5 \times 10^{-3}$, $s = 2.3$, and $\epsilon_e = 0.2$ to reduce the number of free parameters based on the interpretations of the AT 2022cmc X-ray data (C. Yuan et al. 2024b),[11] while we allow $\epsilon_B$ to vary freely for X-ray spectral fittings, as it significantly impacts the cooling frequencies in the synchrotron spectra.

Although the RS scenarios have been shown to describe the X-ray afterglows of jetted TDEs, and FS emissions are subdominant in X-ray ranges, we include here the contribution from FS regions for completeness. Instead of introducing new free parameters, we follow the treatment in C. Yuan et al. (2024b) and apply the FS parameters obtained from the AT 2022cmc radio data fitting to all four jetted TDEs.

[11] These values are also consistent with values suggested by the RS model for early GRB afterglow emission (F. Genet et al. 2007).

Applying the model described in Section 2 to X-ray light curves and spectra in the energy range of 0.3–10 keV for AT 2022cmc, Sw J1644, Sw J2058, and Sw J1112, we obtain the fitting parameters, as shown in Table 1, where the characteristic times $T_{\rm fb}$ and $T_{\rm br}$ are also shown. Figure 1 illustrates the fit of X-ray light curves. The black dashed curves show the X-ray light curves predicted by the RS scenario with jet break corrections. The numerical results are consistent with the analytical RS light curves at $E_X \sim 1$ keV (C. Yuan et al. 2024b),

$$\nu F_\nu \propto \begin{cases} f_{\rm br} T_{\rm obs}^{-[5\alpha+\alpha(s-1)]/4}, & T_{\rm obs} < T_{\rm fb} \\ f_{\rm br} T_{\rm obs}^{-(2s+25)/12}, & T_{\rm obs} > T_{\rm fb}. \end{cases} \quad (5)$$

From this figure, we observe that the RS model with jet break steepening can describe the X-ray afterglows of AT 2022cmc and Sw J1112, encompassing both the early-stage observations and the late-time upper limits. However, for Sw J1644 and Sw J2058, the late-time X-ray emissions from the RS model exceed the upper limits (see the corresponding dashed black curves), indicating that a sharper decay is required.

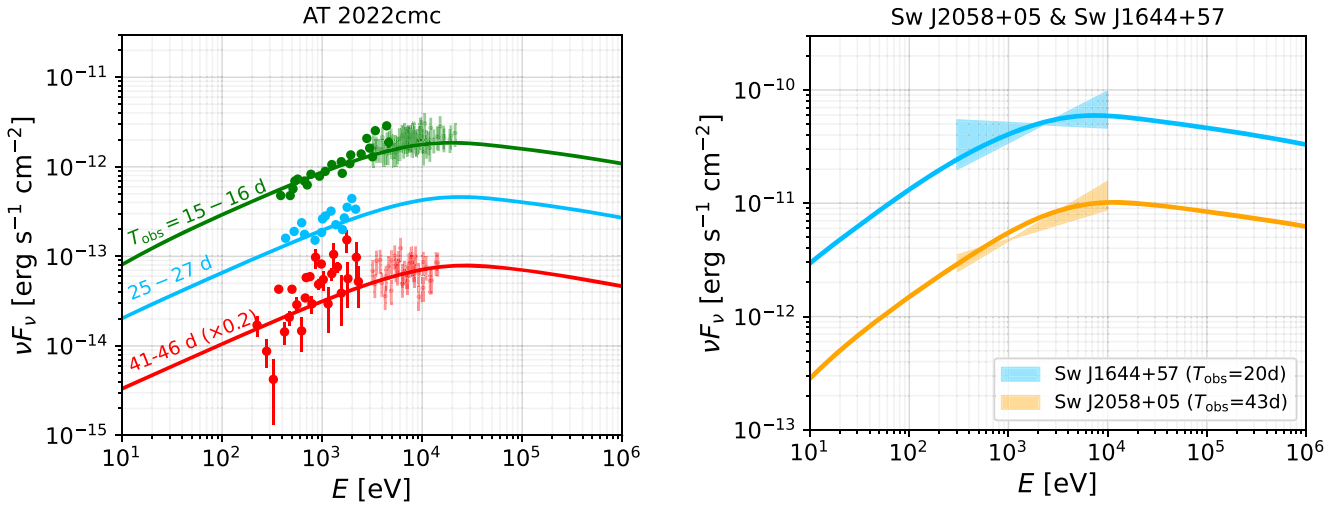


**Figure 2.** X-ray spectra fitting for AT 2022cm (left panel), J1644 and J2058 (right panel) at different times. The data sources are the same as those of Figure 1.

To address this issue, we introduce the ceased central engine mechanism by turning off the jet power injection $L_j$ after $T_{ce}=(1+z)t_{ce}$, as the accretion rate becomes sub-Eddington (B. A. Zauderer et al. 2013; A. Tchekhovskoy et al. 2014). The cessation time $t_{ce}$ is determined by $\dot{M}_{BH}(t_{ce})=L_{Edd}/(\eta_{rad}c^2)$, where $L_{Edd}\simeq 1.3\times10^{45}$ erg s$^{-1}M_{BH,7}$ is the Eddington luminosity and $\eta_{rad}$ is the radiation efficiency. Explicitly, we write down

$$t_{ce}=\left(\frac{\eta_{acc}\eta_{rad}M_\star c^2}{\mathcal{C}CL_{Edd}t_{fb}}\right)^{3/5}t_{fb}$$
$$\simeq 134 \quad \mathrm{d} \quad M_{\star,0.7}^{14/25}M_{BH,7}^{-2/5} \qquad (6)$$

for $\alpha=0.8$ and $\eta_{acc}\eta_{rad}=0.05$. Table 1 summarizes $T_{ce}$ for each TDE, using $\eta_{acc}\eta_{rad}=0.05$ as the fiducial parameter. Physically, after $t_{ce}$, the RS emission decays rapidly, as the ceased central engine suspends the electron injection once the shock crossing is complete. The solid black curves in Figure 1 illustrate the light curves after shutting down the power injection following $T_{ce}$, while the gray dashed lines correspond to the cessation times for each TDE. We conclude that the RS model, incorporating jet break steepening and the ceased central engine mechanism, effectively explains the rapid decay observed in the late-stage X-ray light curves, particularly for Sw J2058 and Sw J1644. In both cases, the FS contributions are subdominant as pointed out by C. Yuan et al. (2024b) for AT 2022 cmc.

In the early stage when the jet is still in the coasting phase, the X-ray fluxes increase with time as the RS begins to cross the ejecta. This feature explains the peaks observed in the light curves of Sw J1644 and Sw J2058 at $T_{obs}\sim10$ days. The X-ray observations of AT 2022cmc at $T_{obs}\sim4$ days and the fluctuations seen in Sw J1644's light curve at earlier times, e.g., $T_{obs}\lesssim4$ days, may be attributed to internal energy dissipations occurring close to the SMBH (e.g., W.-H. Lei et al. 2013), analogous to the prompt phase of GRBs.

We focus on spectral fitting in the X-ray range, e.g., 0.3–10 keV, as there are no $\gamma$-ray observations for these four jetted TDEs, and the radio observations are typically attributed to FS emissions from a slower jet (e.g., T. Matsumoto & B. D. Metzger 2023; C. Yuan et al. 2024b; C. Zhou et al. 2024, for AT 2022cmc). We present in Figure 2 the fit to X-ray spectra for AT 2022cmc (left panel), and Sw J2058 and Sw J1664 (right panel). The results indicate that the fast cooling synchrotron spectra can reproduce the X-ray spectra in the energy range 0.3–10 keV.

### 3.2. $\gamma$-Ray and Neutrino Detectabilities

The accelerated nonthermal electrons could produce $\gamma$-rays in energy ranges of the Fermi Large Area Telescope (LAT), e.g., 100 MeV to 10 GeV. It is useful to discuss the $\gamma$-ray detectabilities. The left panel of Figure 3 illustrates the time-dependent $\gamma$-ray flux for each jetted TDE. Similar to the X-ray light curves, the $\gamma$-ray light curves exhibit fast-decaying signatures with the peak flux level maintaining over tenths of days. For reference, the 100 day Fermi-LAT sensitivity line (M. Ajello et al. 2021) is also shown as the horizontal gray line. This figure indicates that it is challenging to detect the fast-decaying $\gamma$-ray emissions by Fermi-LAT, which explains the nondetection of these sources in $\gamma$ rays. In the very-high-energy $\gamma$-ray regime, e.g., $\gtrsim$100 GeV–1 TeV, the fluxes are suppressed by the Klein–Nishina effect of inverse Compton radiation and $\gamma\gamma$ attenuation with extragalactic background lights, making these jetted TDEs increasingly challenging to be detected unless the source is nearby and/or additional mechanisms, such as external inverse Compton emission, are introduced.

Recent identification of TDEs and TDE candidates with potential neutrino correlations, e.g., AT 2019dsg (R. Stein et al. 2021), AT 2019fdr (S. Reusch et al. 2022), AT 2019aalc (S. van Velzen et al. 2024), AT 2021lwx (C. Yuan et al. 2024a), ATLAS17jrp (R.-L. Li et al. 2024), and two obscured candidates (N. Jiang et al. 2023), have revealed that TDEs could be promising neutrino emitters. Here, motivated by these observations, we consider neutrino emission from on-axis jetted TDEs. We use the parameters obtained from X-ray data fittings to compute the cumulative single-flavor neutrino fluences from external relativistic shocks of jetted TDEs, which are shown in the right panel of Figure 3. Neutrino mixing in a vacuum is assumed. In this calculation, we consider an optimistic case where one-third of the jet kinetic power is converted to the accelerated protons (e.g., $\epsilon_p=L_p/L_j=1/3$) and treat the synchrotron emissions as the target photon field for $p\gamma$ interactions. For simplicity, we assume a power-law proton injection spectrum $\dot{Q}_p\propto E_p^{-2}\exp(-E_p/E_{p,max})$ and

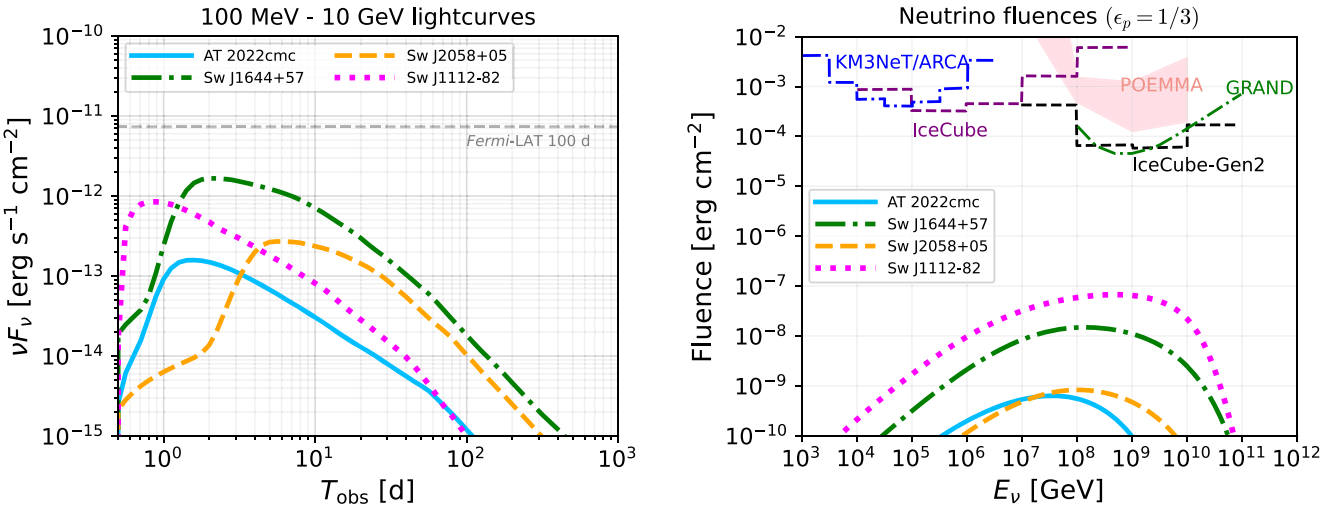


**Figure 3.** Left panel: model-predicted 100 MeV–10 GeV $\gamma$-ray light curves for each TDE. The horizontal dashed line indicates the Fermi-LAT sensitivity for 100 day observations. Right panel: expected single-flavor neutrino fluences originated from the external FS and RS regions. Optimistic proton acceleration efficiency of $\epsilon_p = 1/3$ is used. In both calculations, the parameters obtained from X-ray data fits are applied. See the main text for a detailed description of the sensitivity curves.

determine the maximum energy $E_{p,\max}$ by equating the acceleration time to the cooling time.

In the right panel of Figure 3, the sensitivity curves of IceCube (decl. $\delta = -23^\circ$), IceCube-Gen2 ($\delta = 0^\circ$; R. Abbasi et al. 2021), GRAND (zenith angle $\theta = 90^\circ$; J. Álvarez-Muñiz et al. 2020), KM3NeT/ARCA230 ($\delta = -73^\circ$; S. Aiello et al. 2024), and POEMMA (90% unified confidence level; T. M. Venters et al. 2020) are also shown. We find that the neutrino fluences from these jetted TDEs are at least 2 orders of magnitude lower than the IceCube-Gen2 sensitivity. The major reason is that the jetted TDEs are fast-fading transients compared to persistent AGNs, and the $p\gamma$ interaction efficiencies in the jets of radii $R_j \gtrsim 10^{18}$ cm are low unless a substantial number of external target photons are introduced. Compact jet, internal energy dissipations, external target photons, and/or dense external media (e.g., M. Klinger et al. 2024b) would be needed to make jetted TDEs promising neutrino emitters.

We also note that our model would not explain neutrino events from AT 2019dsg, AT 2019fdr, AT 2019aalc, and AT 2021lwx because the fluences are too small. In addition, these TDEs are not on-axis jetted TDEs and the jet energy is constrained by afterglow observations (K. Murase et al. 2020), although the constraints are relaxed hidden jets with time delays (M. Mukhopadhyay et al. 2024).

## 4. Discussion

We have presented the RS model incorporating continuously powered jets to explain the X-ray afterglows of four jetted TDEs: AT 2022cmc, Sw J1644, Sw J2058, and Sw J1112. Concerning the number of free parameters, we observe that by fixing $f_e = 1.5 \times 10^{-3}$, $s = 2.3$, $\epsilon_e = 0.2$, and $k = 1.8$, the spectral and light-curve fitting reduces the degeneracy of the parameters. For instance, $\alpha$ determines the light-curve slopes before $T_{\rm fb}$, while $\mathcal{E}_j$ normalizes the X-ray luminosities. The parameters $n_{\rm ISM}$ and $\Gamma_0$ jointly define the jet deceleration time and the light-curve peaks, and $\theta_j$ controls the jet break time $T_{\rm br}$, whereas the cooling frequencies of X-ray spectra depend strongly on $\epsilon_B$. Moreover, by adopting the typical value $\eta_{\rm acc}\eta_{\rm j} \sim 0.02$, we infer that the masses of the disrupted stars are distributed in the range 1.6–3.5$M_\odot$ (see Table 1), which is consistent with the limits estimated from optical/radio observations.

In addition to the rapid decays, another significant feature of the observed X-ray light curves of the four jetted TDEs, especially Sw J1644, is their rapid variability of $\sim$a few $\times$ 100–1000 s. The variability timescale of homogeneous RS downstreams is typically close to the observation time, e.g., $T_{\rm rs,var} \sim (1+z)R_j/(\Gamma^2 c) \sim T_{\rm obs}$. Since the jet is continuously powered by the SMBH, the observed variability time is modulated by the light-crossing time of the central engine (K. Ioka et al. 2005; R. C. Reis et al. 2012). Moreover, the stochastic magnetic dissipation (B. Zhang & H. Yan 2011) and small-scale plasma fluctuations may also cause short-term variabilities. On the other hand, the X-ray light curves also exhibit some quasiperiodic (1–10 days) variation, with dips that cannot be simply attributed to external shock evolution. These short-term structures may be caused by jet precessions induced by misaligned accretion disks (C. J. Saxton et al. 2012; N. Stone & A. Loeb 2012; W.-H. Lei et al. 2013; D. Calderón et al. 2024); however, a quantitative modeling of these effects is beyond the scope of this work.

Besides the RS emission, contributions from the FS region are also included in our calculations and are found to be negligible in X-ray bands using the same parameters for radio data fitting, which disfavors the external FS as the origin of jetted TDE X-ray emission. This also supports the two-component jet model, suggesting that the FS in slow ($\Gamma_0 \sim$ 1–10) jets and the RS in fast ($\Gamma_0 > 10$) jets explain the radio and X-ray observations (C. Yuan et al. 2024b), respectively.

## 5. Conclusions

We modeled the jet evolution within an external density medium by connecting the CNM profile, e.g., $n_{\rm cnm} \propto R^{-k}$, to the ISM, and computed the time-dependent synchrotron and SSC emission from RS regions. We concluded that the external RS model for the jet may provide a generic and self-consistent framework to explain the baselines of the X-ray afterglows of jetted TDEs: Sw J1644, Sw J2058, Sw J1112, and AT 2022cmc. Remarkably, the jet break, together with a ceased central engine when the accretion rate falls below the

Eddington accretion rate, could explain the sharp declines in the late-stage X-ray light curves, especially for Sw J1644 and Sw J2058.

Our work also predicts the peak $\gamma$-ray flux to be $\lesssim 2\times 10^{-12}\,\mathrm{erg\,s^{-1}\,cm^{-2}}$ (see the left panel of Figure 3), which is lower than the Fermi-LAT 100 day sensitivity and explains the nondetection of $\gamma$-rays from jetted TDEs. Moreover, choosing an optimistic proton acceleration efficiency of $\epsilon_p = L_p/L_j = 1/3$, the neutrino fluences from the four jetted TDEs are still more than 2 orders of magnitude lower than the IceCube-Gen2 sensitivity.

Future work incorporating external RSs, periodic jet precessions, and the contribution of internal energy dissipations would offer a more comprehensive description of the TDE X-ray afterglows, reproducing simultaneously the overall slopes, short-term fluctuations, and rapid variability.

## Acknowledgments

We would like to thank Brian Metzger for useful discussions, and Damiano Fiorillo for useful comments on this manuscript. The work of K.M. is supported by the NSF grant Nos. AST-2108466, AST-2108467, and AST-2308021, and the JSPS KAKENHI grant No. 20H05852.

*Software:* NumPy (C. R. Harris et al. 2020), Matplotlib (J. D. Hunter 2007), pybind11 (W. Jakob et al. 2017), Eigen (G. Guennebaud et al. 2010), AM$^3$ (M. Klinger et al. 2024a).

## Appendix
## Time-dependent RS Emissions

Given the minimum electron Lorentz factor, $\gamma_{e,\mathrm{m}} = (\Gamma_{\mathrm{rel}} - 1)g(s)(\epsilon_e/f_e)(m_p/m_e)$, we normalize the electron injection rate $\dot{Q}_e$ via

$$(4\pi R_j^2 t'_{\mathrm{dyn}} c)\int \dot{Q}_e d\gamma_e = \frac{f_e L_{j,iso}}{\Gamma_0 m_p c^2}, \tag{A1}$$

where $t'_{\mathrm{dyn}} = R_j/(\Gamma c)$ is the comoving dynamic time, $g(s) = (s-2)/(s-1)$ for $s > 2$ and $g(s) \sim \mathcal{O}(0.1)$ for $s = 2$.

We use the AM$^3$ software (M. Klinger et al. 2024a) to model the time-dependent synchrotron and inverse Compton emissions in the SSC framework by numerically solving the transport equations for electrons and photons in the comoving frame, specifically, for electrons,

$$\frac{\partial n'_e}{\partial t'} = \dot{Q}_e - \frac{\partial}{\partial \gamma_e}(\dot{\gamma}_e n'_e) - \frac{n'_e}{t'_{\mathrm{dyn}}}, \tag{A2}$$

where $n'_e$ is the electron number density (differential in Lorentz factor and volume), $t'$ is the time measured in comoving frame, and $\dot{\gamma}_e$ is the electron energy loss rate due to synchrotron radiation, inverse Compton scattering, and adiabatic cooling. In this calculation, we self-consistently determine the maximum electron Lorentz factor by equating the acceleration rate $t'^{-1}_{\mathrm{acc}} = eB_{\mathrm{rs}}/(\gamma_e m_e c)$ to the cooling rate $t'^{-1}_{c} = |\dot{\gamma}_e|/\gamma_e$.

To obtain the observed photon spectra and light curves, we convert the comoving photon density spectra $n'_\gamma$ (in the units of $\mathrm{cm^{-3}}$) to the flux in the observer's frame by integrating over the equal-arrival-time surfaces (e.g., K. Takahashi et al. 2022; Y. Sato et al. 2024; B. T. Zhang et al. 2025),

$$F(E, T_{\mathrm{obs}}) = \frac{2\pi(1+z)}{d_L^2}\int_0^{\theta_j} d\theta \sin(\theta) R_j^2 \times \Delta R_j f_{\mathrm{br}} \frac{j'(\hat{t}, R_j, \varepsilon')}{\Gamma^2(1-\beta\mu)^2}\Bigg|_{\hat{t}=\frac{T_{\mathrm{obs}}}{1+z}+\frac{\mu R_j}{c}}, \tag{A3}$$

where $j' = n'_\gamma/(4\pi t'_{\mathrm{dyn}})$ is the emissivity per unit solid angle, $\hat{t}$ is the emission time, $\mu = \cos\theta$, $\beta = \sqrt{1-1/\Gamma^2}$, $\beta_{\mathrm{sh}} = \sqrt{1-1/\Gamma_{\mathrm{sh}}^2}$ is the shock velocity with $\Gamma_{\mathrm{sh}} = \sqrt{2}\Gamma$. In this expression, $\varepsilon' = (1+z)E/\Gamma$ connects the energy in the observer's frame ($E$) to energy in the comoving frame ($\varepsilon'$), and $\Delta R_j = R_j/[12\Gamma^2(1-\mu\beta_{\mathrm{sh}})]$ (K. Takahashi et al. 2022) measures the radical thickness of the shocked region that contributes to the observed flux at $T_{\mathrm{obs}}$. The jet break correction factor $f_{\mathrm{br}} = 1/[1 + (\theta_j\Gamma)^{-2}]$ is also included.

## ORCID iDs

Chengchao Yuan (袁成超) https://orcid.org/0000-0003-0327-6136
Walter Winter https://orcid.org/0000-0001-7062-0289
B. Theodore Zhang (张兵) https://orcid.org/0000-0003-2478-333X
Kohta Murase https://orcid.org/0000-0002-5358-5642
Bing Zhang (张冰) https://orcid.org/0000-0002-9725-2524

## References

Abbasi, R., Ackermann, M., Adams, J., et al. 2021, ICRC (Berlin), 37, 1183
Aiello, S., Albert, A., Alshamsi, M., et al. 2024, ApJ, 162, 102990
Ajello, M., Atwood, W. B., Axelsson, M., et al. 2021, ApJS, 256, 12
Alexander, K. D., van Velzen, S., Horesh, A., & Zauderer, B. A. 2020, SSRv, 216, 81
Álvarez-Muñiz, J., Alves Batista, R., Balagopal, V. A., et al. 2020, SCPMA, 63, 219501
Andreoni, I., Coughlin, M. W., Perley, D. A., et al. 2022, Natur, 612, 430
Berger, E., Zauderer, A., Pooley, G. G., et al. 2012, ApJ, 748, 36
Bloom, J. S., Giannios, D., Metzger, B. D., et al. 2011, Sci, 333, 203
Brown, G. C., Levan, A. J., Stanway, E. R., et al. 2015, MNRAS, 452, 4297
Brown, G. C., Levan, A. J., Stanway, E. R., et al. 2017, MNRAS, 472, 4469
Burrows, D., Kennea, J., Ghisellini, G., et al. 2011, Natur, 476, 421
Calderón, D., Pejcha, O., Metzger, B. D., & Duffell, P. C. 2024, MNRAS, 528, 2568
Cendes, Y., Eftekhari, T., Berger, E., & Polisensky, E. 2021, ApJ, 908, 125
Cenko, S. B., Krimm, H. A., Horesh, A., et al. 2012, ApJ, 753, 77
Crumley, P., Lu, W., Santana, R., et al. 2016, MNRAS, 460, 396
Dai, J. L., Lodato, G., & Cheng, R. 2021, SSRv, 217, 12
De Colle, F., & Lu, W. 2020, NewAR, 89, 101538
Eftekhari, T., Berger, E., Zauderer, B. A., Margutti, R., & Alexander, K. D. 2018, ApJ, 854, 86
Eftekhari, T., Tchekhovskoy, A., Alexander, K. D., et al. 2024, ApJ, 974, 149
Evans, C. R., & Kochanek, C. S. 1989, ApJL, 346, L13
Genet, F., Daigne, F., & Mochkovitch, R. 2007, MNRAS, 381, 732
Giannios, D., & Metzger, B. D. 2011, MNRAS, 416, 2102
Guennebaud, G., Jacob, B., et al. 2010, Eigen v3, http://eigen.tuxfamily.org
Guillochon, J., & Ramirez-Ruiz, E. 2013, ApJ, 767, 64
Harris, C. R., Millman, K. J., van der Walt, S. J., et al. 2020, Natur, 585, 357
Hills, J. G. 1975, Natur, 254, 295
Hunter, J. D. 2007, CSE, 9, 90
Ioka, K., Kobayashi, S., & Zhang, B. 2005, ApJ, 631, 429
Jakob, W., Rhinelander, J., & Moldovan, D. 2017, pybind11 - Seamless Operability Between C++11 and Python, https://github.com/pybind/pybind11
Jiang, N., Zhou, Z., Zhu, J., Wang, Y., & Wang, T. 2023, ApJL, 953, L12
Kelley, L. Z., Tchekhovskoy, A., & Narayan, R. 2014, MNRAS, 445, 3919
Kippenhahn, R., & Weigert, A. 1990, Stellar Structure and Evolution (Cambridge: Cambridge Univ. Press)

Klinger, M., Rudolph, A., Rodrigues, X., et al. 2024a, ApJS, 275, 4
Klinger, M., Yuan, C., Taylor, A. M., & Winter, W. 2024b, ApJ, 977, 242
Lei, W.-H., Yuan, Q., Zhang, B., & Wang, D. 2016, ApJ, 816, 20
Lei, W.-H., Zhang, B., & Gao, H. 2013, ApJ, 762, 98
Lei, W.-H., Zhang, B., Wu, X.-F., & Liang, E.-W. 2017, ApJ, 849, 47
Levan, A. J., Tanvir, N. R., Cenko, S. B., et al. 2011, Sci, 333, 199
Li, R.-L., Yuan, C., He, H.-N., et al. 2024, arXiv:2411.06440
Liu, D., Pe'er, A., & Loeb, A. 2015, ApJ, 798, 13
Mangano, V., Burrows, D. N., Sbarufatti, B., & Cannizzo, J. K. 2016, ApJ, 817, 103
Matsumoto, T., & Metzger, B. D. 2023, MNRAS, 522, 4028
Matsumoto, T., & Piran, T. 2024, ApJ, 971, 49
Metzger, B. D., Giannios, D., & Mimica, P. 2012, MNRAS, 420, 3528
Mimica, P., Giannios, D., Metzger, B. D., & Aloy, M. A. 2015, MNRAS, 450, 2824
Mukhopadhyay, M., Bhattacharya, M., & Murase, K. 2024, MNRAS, 534, 1528
Murase, K., Kimura, S. S., Zhang, B. T., Oikonomou, F., & Petropoulou, M. 2020, ApJ, 902, 108
Nava, L., Sironi, L., Ghisellini, G., Celotti, A., & Ghirlanda, G. 2013, MNRAS, 433, 2107
Pasham, D. R., Cenko, S. B., Levan, A. J., et al. 2015, ApJ, 805, 68
Pasham, D. R., Lucchini, M., Laskar, T., et al. 2023, NatAs, 7, 88
Phinney, E. S. 1989, in IAU Symp. 136, The Center of the Galaxy, ed. M. Morris (Dordrecht: Kluwer), 543
Piran, T., Svirski, G., Krolik, J., Cheng, R. M., & Shiokawa, H. 2015, ApJ, 806, 164
Rees, M. J. 1988, Natur, 333, 523
Reis, R. C., Miller, J. M., Reynolds, M. T., et al. 2012, Sci, 337, 949
Reusch, S., Stein, R., Kowalski, M., et al. 2022, PhRvL, 128, 221101
Sato, Y., Murase, K., Bhattacharya, M., et al. 2024, PhRvD, 110, L061307
Saxton, C. J., Soria, R., Wu, K., & Kuin, N. P. M. 2012, MNRAS, 422, 1625
Saxton, R., Komossa, S., Auchettl, K., & Jonker, P. G. 2020, SSRv, 216, 85
Shen, R.-F., & Matzner, C. D. 2014, ApJ, 784, 87
Stein, R., van Velzen, S., Kowalski, M., et al. 2021, NatAs, 5, 510
Stone, N., & Loeb, A. 2012, PhRvL, 108, 061302
Takahashi, K., Ioka, K., Ohira, Y., & van Eerten, H. J. 2022, MNRAS, 517, 5541
Tchekhovskoy, A., Metzger, B. D., Giannios, D., & Kelley, L. Z. 2014, MNRAS, 437, 2744
Teboul, O., & Metzger, B. D. 2023, ApJL, 957, L9
van Velzen, S., Gezari, S., Hammerstein, E., et al. 2021, ApJ, 908, 4
van Velzen, S., Stein, R., Gilfanov, M., et al. 2024, MNRAS, 529, 2559
Venters, T. M., Reno, M. H., Krizmanic, J. F., et al. 2020, PhRvD, 102, 123013
Wang, F. Y., & Cheng, K. S. 2012, MNRAS, 421, 908
Wang, J.-Z., Lei, W.-H., Wang, D.-X., et al. 2014, ApJ, 788, 32
Yao, Y., Lu, W., Harrison, F., et al. 2024, ApJ, 965, 39
Yuan, C., Murase, K., Kimura, S. S., & Mészáros, P. 2020, PhRvD, 102, 083013
Yuan, C., Murase, K., Zhang, B. T., Kimura, S. S., & Mészáros, P. 2021, ApJL, 911, L15
Yuan, C., Winter, W., & Lunardini, C. 2024a, ApJ, 969, 136
Yuan, C., Zhang, B. T., Winter, W., & Murase, K. 2024b, ApJ, 974, 162
Yuan, Q., Wang, Q. D., Lei, W.-H., Gao, H., & Zhang, B. 2016, MNRAS, 461, 3375
Zauderer, B. A., Berger, E., Margutti, R., et al. 2013, ApJ, 767, 152
Zauderer, B. A., Berger, E., Soderberg, A. M., et al. 2011, Natur, 476, 425
Zhang, B. 2018, The Physics of Gamma-ray Bursts (Cambridge: Cambridge Univ. Press)
Zhang, B., & Yan, H. 2011, ApJ, 726, 90
Zhang, B. T., Murase, K., Ioka, K., & Zhang, B. 2025, JHEAp, 45, 392
Zhou, C., Zhu, Z.-P., Lei, W.-H., et al. 2024, ApJ, 963, 66
Zou, Y. C., Wang, F. Y., & Cheng, K. S. 2013, MNRAS, 434, 3463